Giant All-Optical Modulation of Second-Harmonic Generation Mediated by Dark Excitons

Yadong Wang[#], Susobhan Das[#], Fadil Iyikanat[#], Yunyun Dai, Shisheng Li, Xiangdong Guo, Xiaoxia Yang, Jinluo Cheng, Xuerong Hu, Masood Ghotbi, Fangwei Ye, Harri Lipsanen, Shiwei Wu, Tawfique Hasan, Xuetao Gan, Kaihui Liu, Dong Sun, Qing Dai, F. Javier García de Abajo*, Jianlin Zhao*, and Zhipei Sun*

Corresponding Authors

F. Javier García de Abajo - *ICFO-Institut de Ciencies Fotoniques, The Barcelona Institute of Science and Technology, 08860 Castelldefels (Barcelona), Spain*; *ICREA-Institució Catalana de Recerca i Estudis Avançats, Passeig Lluís Companys 23, 08010 Barcelona, Spain*; Email: javier.garciadeabajo@nanophotonics.es

Jianlin Zhao - *MOE Key Laboratory of Material Physics and Chemistry under Extraordinary Conditions, and Shaanxi Key Laboratory of Optical Information Technology, School of Physical Science and Technology, Northwestern Polytechnical University, Xi'an 710129, China*; Email: jlzhao@nwpu.edu.cn

Zhipei Sun - *Department of Electronics and Nanoengineering, Aalto University, Espoo 02150, Finland*; *QTF Centre of Excellence, Department of Applied Physics, Aalto University, Espoo 02150, Finland*; https://orcid.org/0000-0002-9771-5293; Email: zhipei.sun@aalto.fi

Authors

Yadong Wang - *MOE Key Laboratory of Material Physics and Chemistry under Extraordinary Conditions, and Shaanxi Key Laboratory of Optical Information Technology, School of Physical Science and Technology, Northwestern Polytechnical University, Xi'an 710129, China*; *Department of Electronics and Nanoengineering, Aalto University, Espoo 02150, Finland*; https://orcid.org/0000-0001-8603-3468

Susobhan Das - *Department of Electronics and Nanoengineering, Aalto University, Espoo 02150, Finland*

Fadil Iyikanat - *ICFO-Institut de Ciencies Fotoniques, The Barcelona Institute of Science and Technology, 08860 Castelldefels (Barcelona), Spain*

Yunyun Dai - *Department of Electronics and Nanoengineering, Aalto University, Espoo 02150, Finland*; https://orcid.org/0000-0002-1186-1864

Shisheng Li - *International Center for Young Scientists, National Institute for Materials Science, Tsukuba 305-0044, Japan*

Xiangdong Guo - *CAS Key Laboratory of Nanophotonic Materials and Devices, CAS Key Laboratory of Standardization and Measurement for Nanotechnology, CAS Center for Excellence in Nanoscience, National Center for Nanoscience and Technology, Beijing 100190, China*

Xiaoxia Yang - *CAS Key Laboratory of Nanophotonic Materials and Devices, CAS Key Laboratory of Standardization and Measurement for Nanotechnology, CAS Center for Excellence in Nanoscience, National Center for Nanoscience and Technology, Beijing 100190, China*

Jinluo Cheng - *Changchun Institute of Optics, Fine Mechanics and Physics, Chinese Academy of Sciences, Changchun, Jilin 130033, China*; https://orcid.org/0000-0003-4875-9342

Xuerong Hu - *Department of Electronics and Nanoengineering, Aalto University, Espoo 02150, Finland*; *International Cooperation Base of Photoelectric Technology and Functional Materials, and Institute of Photonics and Photon-Technology, Northwest University, Xi'an 710069, China*

Masood Ghotbi - *Department of Physics, University of Kurdistan, Pasdaran St., Sanandaj 66177-15177, Iran*

Fangwei Ye - *School of Physics and Astronomy, Shanghai Jiao Tong University, Shanghai 200240, China*

Harri Lipsanen - *Department of Electronics and Nanoengineering, Aalto University, Espoo 02150, Finland*; https://orcid.org/0000-0003-2487-4645

Shiwei Wu - *State Key Laboratory of Surface Physics, Key Laboratory of Micro and Nano Photonic Structures (MOE), and Department of Physics, Fudan University, Shanghai 200433, China*; https://orcid.org/0000-0001-9838-9066

Tawfique Hasan - *Cambridge Graphene Centre, University of Cambridge, Cambridge CB3 0FA, United Kingdom*; https://orcid.org/0000-0002-6250-7582

Xuetao Gan - *MOE Key Laboratory of Material Physics and Chemistry under Extraordinary Conditions, and Shaanxi Key Laboratory of Optical Information Technology, School of Physical Science and Technology, Northwestern Polytechnical University, Xi'an 710129, China*; https://orcid.org/0000-0003-2469-5807

Kaihui Liu - *State Key Laboratory for Mesoscopic Physics and School of Physics, Peking University, Beijing 100871, China*

Dong Sun - *International Center for Quantum Materials, School of Physics, Peking University, Beijing 100871, China*; https://orcid.org/0000-0002-0898-4548

Qing Dai - *CAS Key Laboratory of Nanophotonic Materials and Devices, CAS Key Laboratory of Standardization and Measurement for Nanotechnology, CAS Center for Excellence in Nanoscience, National Center for Nanoscience and Technology, Beijing 100190, China*; https://orcid.org/0000-0002-1750-0867

Abstract:

All-optical control of nonlinear photonic processes in nanomaterials is of significant interest from a fundamental viewpoint and with regard to applications ranging from ultrafast data processing to spectroscopy and quantum technology. However, these applications rely on a high degree of control over the nonlinear response, which still remains elusive. Here, we demonstrate giant and broadband all-optical ultrafast modulation of second-harmonic generation (SHG) in monolayer transition-metal dichalcogenides mediated by the modified excitonic oscillation strength produced upon optical pumping. We reveal a dominant role of dark excitons to enhance SHG by up to a factor of ~386 at room temperature, 2 orders of magnitude larger than the current state-of-the-art all-optical modulation results. The amplitude and sign of the observed

SHG modulation can be adjusted over a broad spectral range spanning a few electronvolts with ultrafast response down to the sub-picosecond scale via different carrier dynamics. Our results not only introduce an efficient method to study intriguing exciton dynamics, but also reveal a new mechanism involving dark excitons to regulate all-optical nonlinear photonics.

KEYWORDS: Second-Harmonic Generation, Dark Excitons, Bright Excitons, Transition Metal Dichalcogenides Monolayers, Ultrafast Optical Modulation, Optically-Modulated Excitonic Strength

Introduction

Second-harmonic generation (SHG), a nonlinear optical process originating in the second-order response of noncentrosymmetric materials, is arguably the most commonly used nonlinear optical effect.[1] An efficient control of SHG is vital for various important applications that include optical data processing, spectroscopy, and quantum photonics. In previous works, all-optical control of SHG[2] has been demonstrated in semiconductors[3] as well as in metallic[4] and hybrid structures,[5–7] primarily relying on optically induced electric fields and hot electrons. However, the reported modulation of SHG in noncentrosymmetric materials is generally very weak (typically with enhancement factors $\lesssim 4$). This lack of efficient all-optical modulation strategies represents a major bottleneck toward the development of emerging and future applications, such as quantum photonics and on-chip nonlinear devices.

In recent years, two-dimensional (2D) transition metal dichalcogenides (TMDs) have emerged as a powerful platform for applications in photonics and optoelectronics,[8] including nonlinear optics.[9] Specifically, excitons introduce strong resonances in the optical response of TMDs, which dominate their linear and nonlinear optical properties aided by the extreme quantum confinement and reduced screening in these materials.[9–12] As a consequence, significant research efforts have been devoted to investigate and exploit the enhancement of the nonlinear optical response in TMDs,[13–21] which is fascinating from both fundamental and applied perspectives. Interestingly, excitonic Rydberg states exhibit general characteristics of hydrogen-like atoms, possessing a series of discrete optically accessible (bright; 1*s*, 2*s*, ...) and optically forbidden (dark; 2*p*, 3*p*, ...) states, as determined by optical selection rules.[22] Through strong resonant enhancement of bright excitons, SHG can be actively tuned using several methods, such as electrical and chemical doping.[19–21,23–27] However, the influence of dark exciton states on nonlinear optics has remained largely unexploited.[22,28]

Here, we demonstrate giant all-optical modulation of SHG within a broad spectral range in monolayer TMDs at ultrafast speed (down to ~500 fs). Our results confirm that SHG

modulation is strongly related to dark excitonic states, with the SHG modulation being enhanced by the creation of dark excitons and suppressed by bright excitons. The measured enhancement of SHG reaches a factor as large as ~386. By combining bright- and dark-exciton resonances, we achieve a dramatic modulation of the SHG amplitude, sign, and response time over a wide spectral range. We explain our results by performing first-principles calculations supporting the leading role of optically pumped dark excitons. Our study emphasizes time-resolved SHG spectroscopy as an efficient way to investigate high-order excitonic states and their dynamics in 2D materials and their heterostructures. Additionally, our demonstration of a giant enhancement in the nonlinear optical processes of TMD materials holds great potential for applications in all-optical devices.

Results and Discussion

Figure 1a shows the schematic of our characterization setup, by which we study the SHG produced by seed light pulses as a function of delay time $\Delta\tau$ with respect to control light pulses in monolayer MoS_2. All experiments are performed at ambient conditions (details in Methods and Supporting Information, SI). We present a typical SHG modulation result in Figure 1b. A readily available control light of photon energy $\hbar\omega_c \approx 3.1$ eV ($\lambda_c \approx 400$ nm wavelength) above the C-exciton peak is chosen. The SHG signal at $\hbar\omega_{SHG} \approx 2.36$ eV ($\lambda_{SHG} \approx 525$ nm) generated by the seed light at $\hbar\omega_s \approx 1.18$ eV ($\lambda_s \approx 1050$ nm) is immediately enhanced by the control light with a single-exponential rising time constant ($\tau_0 \approx 600$ fs, orange fitted line in Figure 1b). After $\Delta\tau \approx 1.3$ ps, the SHG intensity starts to decay, exhibiting two exponential time constants ($\tau_1 \approx 4.4$ ps and $\tau_2 \approx 33$ ps, red fitted curve in Figure 1b). The dynamics at different seed/control light powers (see Figure S3 in the SI) are similar to those shown in Figure 1b. The measured SHG spectra at $\Delta\tau = -1$ and 1.3 ps are shown in Figure 1c, which reveals a strong SHG enhancement produced by the control light.

Figure 1d shows the enhancement factor γ at $\Delta\tau = 1.3$ ps, where a maximum SHG signal is achieved, as a function of the control and seed light powers. We define the enhancement factor as $\gamma = P_w/P_{wo}$, where P_w and P_{wo} are the second harmonic (SH)

powers measured with and without the control light, respectively. We find that γ is highly dependent on the incident light power. Figure 1e represents γ as a function of control light power when the average seed light power (peak intensity) is ∼2 μW (∼21.9 GW/cm^2). We find that γ increases linearly with the control light power (P_c) and is slightly saturated for P_c > 0.4 μW (corresponding to a light intensity of >3.43 GW/cm^2, equivalent to an electron–hole (*e*-*h*) pair density of >5.7 × 10^{14} cm^{-2} when considering the measured absorption of ∼7.1% at ∼3.1 eV). In Figure 1e, we find that γ reaches a maximum value of 386 (with a corresponding enhancement of ∼19 times in second-order nonlinear optical susceptibility), which is ∼2 orders of magnitude larger than previously reported all-optical SHG enhancement results.[6,13−16,19−21,29] We remark that the control light intensity is only ∼4.29 GW/cm^2, that is, ∼5 times less than the seed light intensity of ∼21.9 GW/cm^2. This is notable as the control light power is typically larger than the seed light power in the previously reported results.[30] Similar enhancement phenomena (see Figure S3b in the SI) are observed when the control light energy is changed to ∼1.55 eV (λ_c= 800 nm). The maximum achievable γ at this lower photon energy of the control light is 75, that is, ∼5 times smaller than the results obtained with the 3.1 eV control light (Figure 1d). A higher incident control light power is required at 1.55 eV because it involves two-photon excitations. We have reliably repeated these results using different MoS_2 flakes at ambient conditions with no observable change or damage. Larger γ is achieved with higher control power, as indicated in Figures 1d and S3b, although this results in gradual sample damage during the experiments.

Furthermore, we characterize the valley selection rule. By employing left-circularly polarized (σ−) seed light at ∼1.18 eV, the SH spectra filtered with σ– and σ+ polarizations show ∼96% helicity contrast (see Figure S10b in the SI), confirming the valley selection rule from the D_{3h} crystal symmetry (see the SI, Section 10).[21] When switching the control light on and off, the polarization directions of SHG after passing a quarter-wave plate are almost the same with only ±2° variation (fitted parameters, Figure 1f), indicating that only σ+ polarized SHG is enhanced. This proves that symmetry remains conserved in the presence of control light excitation.

To explore the modulation mechanism, we measure the temporally and spectrally resolved SHG fractional power changes ($\Delta P_{SHG} = (P_w - P_{wo})/P_{wo}$) at different seed energies ($\hbar\omega_s$ from −0.92 to 1.44 eV) with a fixed control light energy of 1.55 eV. We note that the normalized time-resolved SHG dynamics with control light at 1.55 eV is similar to that observed at 3.1 eV (see Figure S4a in the SI). The former one allows us to precisely determine the zero-delay time by sum frequency generation in MoS_2 (see Figure S5 in the SI).

Figure 2a shows a broadband overview of the wavelength dependent SHG modulation dynamics. The SHG is enhanced (i.e., $\Delta P_{SHG} \geq 0$) by the control light when $\hbar\omega_{SHG}$ (λ_{SHG}) lies in the ~2.07–2.56 eV (~598–485 nm) range. We denote this spectral range as the *enhancement region*. A representative result for $\hbar\omega_{SHG} \approx 2.27$ eV is plotted in Figure 2b, showing the dynamics similar to that in Figure 1b. When $\hbar\omega_{SHG}$ is in either the ~2.64–2.88 eV (i.e., ~470–430 nm) or the 1.84–2.07 eV (i.e., ~675–598 nm) range, the SHG is reduced (i.e., $\Delta P_{SHG} \leq 0$) by the control light. We refer to this spectral range as the *suppression region* (Figure 2a). A representative result is shown in Figure 2c for $\hbar\omega_{SHG} \approx 2.85$ eV. In the suppression region, ΔP_{SHG} drops sharply in the presence of control light and reaches its minimum within a delay time $\Delta\tau \approx 150$ fs, faster than our experimental temporal resolution (see Figure S5a in the SI). Then, ΔP_{SHG} recovers with biexponential time constants $\tau_1 \approx 590$ fs and $\tau_2 \approx 96$ ps (see fitting details in Figure S4c in the SI). Within the range lying in between the above-mentioned enhancement and suppression regions in Figure 2a (i.e., ~2.56–2.64 eV), our measurements reveal an extremely fast decay ($\Delta\tau \approx 150$ fs) followed by a fast recovery with a single-exponential time constant of ~600 fs. An example of this behavior with $\hbar\omega_{SHG} \approx 2.58$ eV is offered in Figure 2d. We denote this spectral region as the *transition region*.

In our measurements (Figure 2), the time-resolved dynamics is almost independent of the seed and control light powers (see Figure S3 in the SI), whereas the relative SHG change (ΔP_{SHG}) is linearly related with the control light power in all three regions using the 3.1 eV control light. Therefore, we can rule out an exciton–exciton interaction effect (e.g., exciton–exciton annihilation and Auger recombination), which would commonly

exhibit a nonlinear excitation power dependence. We can thus attribute the SHG modulation effects (i.e., enhancement and suppression) to various excitonic transition processes (e.g., scattering, transition, and recombination) in monolayer MoS_2.

To gain further understanding, we plot ΔP_{SHG} as a function of the SHG photon energy (Figure 3a) for fixed seed and control light intensities with a delay $\Delta\tau \approx 1.3$ ps, where the maximum enhancement is achieved. We find that the minimum dip positions in the suppression region are well correlated with the energies of 1*s*bright exciton states (e.g., $1s_A$, $1s_B$, and $1s_C$, where the subscript denotes the exciton species) in the linear absorption spectrum of monolayer MoS_2 (Figure 3c). We thus attribute the observed suppression of SHG to optical bleaching of bright excitons: the control light excites carriers from the ground state into quasi-continuum states with single-photon excitation processes at 3.1 eV (two-photon excitation at 1.55 eV), and the ground state becomes consequently depleted. This depletion inhibits the formation of bright excitons, blocking the typically observed bright excitonic enhancement effect of SHG and thus reducing the SHG signal.[11] We provide a theoretical quantification of this effect below (see Methods). The bleaching process is typically fast (normally <100 fs),[31,32] which fits well with the dynamics in the suppression region (Figure 2c). The subsequent biexponential recovery process in the suppression region can be correlated with different carrier relaxation processes, which gradually relax to the ground carrier states: an initial period of fast recovery with a characteristic time $\tau_1 \approx 590$ fs can be attributed to carrier cooling dynamics and formation of bright excitons; a subsequent slow recovery with a time constant $\tau_2 \approx 96$ ps can be attributed to carrier-phonon scattering and nonradiative carrier recombination. This biexponential recovery dynamics is similar to what has been previously reported in linear-absorption-based pump–probe measurements on bright excitons.[32,33] We also note that we demonstrate electrical tunability of all-optical suppression of SHG at the $1s_A$ exciton of 1.89 eV (see Figure S9 in the SI), which holds great interest for on-chip electrically tunable all-optical nonlinear device applications. Our results demonstrate that electrical doping suppresses optical modulation, in analogy to electrically tunable SHG.[21] This further confirms that the optically suppressed SHG effect is related to the bright excitons.

Additionally, we observe two strong enhancement peaks at ~2.27 and 2.36 eV in Figure 3a, which are far away from the A and B excitons. We verify that these two enhancement peaks are not featured in either the linear interband absorption spectrum (Figure 3c) or the wavelength-dependent SHG spectrum (see Figure S8in the SI). Furthermore, as shown in the time-resolved results of Figure 2a, the initial rise time of SHG modulation in the enhancement region ($\tau_0 \approx 600$ fs, Figure 2b) is much longer than that in the suppression region (typically ~150 fs, Figure 2c). This indicates a completely different carrier dynamics, which excludes various simultaneous or ultrafast nonlinear effects, including ultrafast optical bleaching and optical parametric interactions. (34) At the same time, we do not observe any change in SHG modulation at 2.27 eV when applying electrical doping (i.e., for a back gate tuning voltage in the −100 to 100 V range). This indicates that electrical doping does not influence the SHG enhancement. In addition, by comparing the normalized SHG polarization dependence in monolayer MoS_2 with and without the control light (see Figure S10a in the SI), we can exclude the possibility of a phase transition during the SHG enhancement process. We also carry out SHG measurements in monolayer WS_2 (see Figures S15 and S16 in the SI). We observe similar enhancement (with a measured γ reaching ~70) and suppression effects in monolayer WS_2, further corroborating the reported all-optical modulation as a general phenomenon in exciton-supporting TMDs. Figure 3b shows ΔP_{SHG} results at a delay time of 2.8 ps (where the maximum enhancement is obtained in Figure S16c in the SI). By comparing with the optical absorption spectral profile in Figure 3d, we assign the dip at ~1.98 eV in the suppression region to an effect involving the bright $1s_A$ state, which also matches well with the PL measurements (see Figure S14 in the SI). In addition, the enhancement region in the ΔP_{SHG}spectrum ranging from ~2.0 to 2.67 eV displays a strong peak at ~2.11 eV and two small peaks at ~2.43 and ~2.58 eV, all of which are not visible in the linear interband absorption spectrum (Figure 3d).

To understand the observed optically driven SHG enhancement, we elaborate a theoretical interpretation of our experimental results in monolayer MoS_2 based on first-principles calculations combined with a phenomenological treatment of optical

pumping. We start by producing accurate calculations of the electronic band structure, as well as the exciton energies and wave functions (see Section S14 in the SI). We then introduce optical pumping through an effective depletion of electrons within an energy interval Δ at the top of the valence band, accompanied by the corresponding filling near the bottom of the conduction band (Figure 4a). The optical transition strengths associated with the excitons are then modified by this redistribution of band occupations, which we directly introduce in the electron–hole-pair (e−h) decomposition of their wave functions (see Methods). This allows us to produce a map of exciton transition strengths resolved in photon energy and band depletion energy Δ (Figure 4b). Spectral variations for selected values of Δ are shown in Figure 4c after introducing a spectral broadening to facilitate comparison to experiment. As the depletion energy increases, we find that the allowed excitations vary considerably: dark excitons with originally low oscillator strength increase their transition dipoles and dominate the optical spectrum, while bright excitons become weaker, in qualitative agreement with the experimental observations. We identify four dominant dark excitons in this process (D_1–D_4), whose real-space wave functions are potted in Figure 4d. We also note that there must be multiple excitations with low oscillator strength that may contribute to the SHG signal, but here we concentrate on the dominant excitations contributing to the observed effects. In addition, assuming that all of the energy absorbed by the material from the control light is invested in producing a depletion Δ (see Methods), we find that the required light intensities are a factor of $\sim$3 lower than those used in experiments (Figure 4b, right scale), which is reasonable in view of the fact that part of that energy can be lost through other dissipative processes (e.g., by spreading the energy among carriers away from the K point).

Supported by these theoretical calculations, we attribute the SHG enhancement to the modified exciton oscillation strength created by a redistribution of excited carriers. In the enhancement region, we propose that some of the carriers in the quasi-continuum of states excited by the control light scatter into low-energy bands and modify the *e*-*h* composition of the excited dark excitonic states, which acquire a substantial transition strength, thus playing a leading role in SHG (Figure 4b, c). We therefore attribute the

rise time (e.g., τ_0 = ~600 fs in Figure 1b) to the remorphing of the *e-h* pair composition of dark excitons. The enhancement decreases due to decay of the excited carrier states with a relatively slow biexponential behavior (e.g., τ_1 = ~2.9 ps and τ_2 = ~325 ps at ~2.27 eV, Figure 2b). We further attribute the fast decay to cooling dynamics of the excited dark excitons, while the slow recovery can be related to carrier-phonon scattering and nonradiative carrier recombination. We note that the decay time in the enhancement region is typically ~10 times longer than the biexponential recovery components in the suppression region induced by bright excitons (Figure 2a, c). This fits well with the results of excited exciton dynamics observed in previous experiments.[22] The leading role played by dark excitons can be further confirmed by comparing the enhancement peak positions with calculated dark exciton energies[35] (see our comparison in Table S2 in the SI) and mid-infrared intraband absorption measurements (see details in Table S1 in the SI). (31) We find that the two enhancement peaks at ~2.27 and ~2.36 eV are likely associated with the 2*p* and 3*p* excitonic states, respectively.

To explain the dynamics in the transition region, we plot time-resolved SHG modulation at different time delays in the ~2.5–2.6 eV spectral range (see Figure S7g in the SI). The results confirm that the time-resolved SHG dynamics (Figure 2d) is governed by the contributions from the suppression and enhancement effects at different time scales: the fast suppression process (<150 fs) in the transition region is initially dominated by bright exciton suppression, similar to the suppression region; then, a relatively slow (~1 ps) enhancement process takes over, similar to the initial response in the enhancement region.

The generality of the dark-exciton mechanism and the dynamics unveiled in this work is further supported by SHG experiments in monolayer WS_2 (Figure 3b; see also Figures S14–S16 in the SI). We assign those peaks in the enhancement region as 2*p*, 3*p*, and 4*p* dark states by comparing with the energies of dark states from refs[28] and[36] (see Table S3 in the SI). This suggests that all-optical modulation of SHG is indeed applicable to other TMDs as well as their heterostructures. We also note that similar modulation effects are possible in other types of nonlinear optical processes,

such as third harmonic generation, optical comb generation, and high harmonic generation, which deserve further investigation.

Although bright excitons (e.g., the 1*s* excitonic state) have been well studied already, dark excitons remain largely unexplored. This is because they are optically forbidden when relying on traditional interband absorption/emission-based pump–probe spectroscopy due to the optical selection rules.[28] Here, thanks to our time-resolved SHG modulation method, we can access dark excitonic states and study their properties (e.g., population dynamics). The demonstrated method features two additional advantages for carrier dynamics exploration: First, its sensitivity is extremely high because the detection parameter of the modulation or change of the SHG signal can be extremely strong. For example, our modulation amplitude (i.e., the change in SHG intensity) is 4 orders of magnitude larger than the variation in the linear absorption (e.g., ~0.2% at ~2.27 eV in MoS_2, as previously reported with traditional pump–probe spectroscopy[37]); secondly, the background noise is low because the detection signal is SHG, thus avoiding the strong probe signal background that is commonly encountered in traditional pump–probe spectroscopy.

Conclusions

We have demonstrated giant all-optical modulation of SHG mediated by excitons in monolayer TMDs. The transient dynamics of excitonic dark and bright states in monolayer MoS_2 has been determined to be the origin of the observed SHG modulation. Thanks to a redistribution of charge carriers produced by a control light beam, dark states acquire a substantial transition strength that contributes to enhance the SHG by a factor as large as 386 in our measurements. In addition, SHG is suppressed by applying electrical gating when the bright excitons are optically bleached. Our results on all-optical modulation of SHG provide a basis for exploiting the unique exciton-photon interactions in 2D materials, while they enable the development of emerging all-optical nonlinear optoelectronic applications.[38,39] For example, the modulation amplitude, sign, and response time can be adjusted over a broad spectral range spanning a few electronvolts (see Figures 2a and S11). We have identified three observed regions with

completely different SHG modulation responses that can potentially enable versatile photonic devices with different functionalities. In particular, an enhancement region that could be utilized for all-optically enhanced nonlinear processes with giant enhancement ratios by applying a relatively low control power. Also, a transition region, in which the large fractional SHG change $|\Delta P_{SHG}|$ (up to 62%, equivalent to the modulation depth of an optical modulator, see Figure S6 in the SI) and the ultrafast fall (<150 fs) and rise (~600 fs) response times could be used for ultrafast all-optical photonic devices, such as all-optical nonlinear modulators. Such a fast response time corresponds to a modulation speed of ~1.4 THz, which is ~14 times faster than that of state-of-the-art electro-optic modulators.[40]

Methods

Material Synthesis and Characterization

Monolayer MoS_2 is grown on a SiO_2/Si substrate by using the chemical vapor deposition method with an ~10 mg sulfur (at 170 °C) and ~0.5/15 mg NaCl/MoO_3 mixture (at 750 °C) for 5 min in high purity argon.[41] Optical characterization of MoS_2, including Raman, photoluminescence, and reflection spectra, can be found in Figure S2 in the SI. A similar method is used to synthesize WS_2, for which characterization is presented in Figure S14 in the SI.

Experimental Methods

In the all-optical modulation experiment, the control and seed light pulses (2 kHz repetition rate) are generated by an optical parametric amplifier (Spectra-Physics, TOPAS) and divided into two parts using a dichroic mirror. The pulse duration of both control and seed pulses is ~230 fs. The seed light goes through an optical delay line and is then combined with the control light by using another dichroic mirror (see Figure S1 in the SI). The combined beams are focused on the sample by a 40× objective of NA 0.75. The full-width-at-half-maximum beam diameters of the control light at 400 nm (800 nm) and the seed light are ~2.5 and ~2.2 μm, respectively. The generated SHG signal is then collected by a monochromator (Andor 328i). Different filters are used to

remove the control and seed light before the monochromator. A photomultiplier tube (PMT, H7844 Hamamatsu) connected to a lock-in amplifier is used to detect and monitor the SHG signal. To calibrate the photon energy dependence, we extract the data after considering the whole system loss within the broad range of used photon energies and the optical reflectance/absorption of both MoS_2 and the substrate.

Theoretical Calculations

We model the pumping-dependent change in the exciton transition strengths from first principles assuming an effective depletion of the valence band produced by the control light. We obtain Kohn–Sham (KS) wave functions and eigenvalues by performing density-functional theory (DFT) calculations using the QUANTUM ESPRESSO code.[42] We then use the Perdew–Burke–Ernzerhof (PBE) version of the generalized gradient approximation (GGA) for the exchange-correlation functional,[43] combined with norm-conserving, fully relativistic pseudopotentials of the Pseudo-Dojo database.[44] The plane-wave energy cutoff is set to 90 Ry for the ground-state calculations. We use the supercell method and include 45 atomic units of vacuum space between two periodic images of the semiconductor layer in order to minimize interactions between adjacent cells. Quasiparticle self-energy corrections to the KS eigenenergies are calculated within the many-body G_0W_0 approximation[45,46] as implemented in the YAMBO code.[47] The absorption spectrum and excitonic effects are obtained by solving the Bethe–Salpeter equation[48,49] (BSE) on top of G_0W_0. The excitonic wave functions are described as $|\Phi^S\rangle = \Sigma_{vck} A_{vck}^S |vck\rangle$, where v and c denote valence and conduction band indices, k runs over wave vectors, A_{vck}^S are expansion coefficients, and S is the exciton index. The excitation energies are determined by solving the BSE equations $(E_{ck} - E_{vk})A_{vck}^S + \Sigma_{v'c'k'}\langle vck|K_{\mathrm{eh}}|v'c'k'\rangle A_{v'c'k'}^S = \Omega^S A_{vck}^S$, where Ω^S is the exciton eigenvalue, E_{vk} and E_{ck} denote the quasiparticle energies of valence and conduction electron band states, respectively, and K_{eh} is the electron–hole interaction kernel. We employ a wave vector grid consisting of $30 \times 30 \times 1$ k points for both G_0W_0 and BSE calculations. The Coulomb cutoff technique is used at the edges of unit cells in the out-of-plane direction.[47] We compute the self-energy and dynamical

dielectric screening using 200 bands. The four highest valence bands and four lowest conduction bands are taken into account in the calculation of excitonic states.(50)

We simulate the optical transition strength in the presence of optical pumping by introducing an effective electron depletion near the top of the valence band, and correspondingly, an occupation near the bottom of the conduction band that preserves charge neutrality. More precisely, we calculate the pumping-dependent transition strength of exciton S using the expression $f_S = |\langle G|\vec{r}|\tilde{\Phi}^S\rangle|^2/|\langle G|\tilde{\Phi}^S\rangle|^2$, where $|G\rangle$ denotes the ground state, whereas $|\tilde{\Phi}^S\rangle = \Sigma_{vck} A_{vck}^S f_{vk}(1 - f_{ck})|vck\rangle$ is the exciton wave function obtained from its electron–hole-pair decomposition coefficients A_{vck}^S and modified by electron redistribution according to the hole and electron occupations f_{vk} and f_{ck} that follow the band filling scheme shown in Figure 4a. For each given value of the valence depletion energy Δ, the conduction filling Δ' is obtained by imposing charge neutrality through $\int_{\mathrm{CBM}}^{\mathrm{CBM}+\Delta'} \mathrm{d}E_{ck}\rho_{Eck} = \int_{\mathrm{VBM}-\Delta}^{\mathrm{VBM}} \mathrm{d}E_{vk}\rho_{Evk}$, where VBM and CBM correspond to the valence band maximum and conduction band minimum, respectively, and $\rho_{E\mathrm{ck}}$ and $\rho_{E\mathrm{vk}}$ are the conduction and valence band densities of states, respectively. The depletion Δ is approximately related to the pumping light intensity I_0through the expression $\int_{\mathrm{CBM}}^{\mathrm{CBM}+\Delta'} \mathrm{d}E_{ck}E_{ck}\rho_{Eck} - \int_{\mathrm{VBM}-\Delta}^{\mathrm{VBM}} \mathrm{d}E_{vk}E_{vk}\rho_{Evk} = I_0 A\tau_{\mathrm{eff}}$, where A is the absorbance calculated at the pump energy $\hbar\omega_{\mathrm{p}} = 3.1$ eV and τ_{eff} is an effective electron–hole recombination time, which we set to an estimated value of 4 ps.(51)

Author Contributions

Y.W., S.D., and F.I. contributed equally to this paper. Y.W. and Z.S. conceived the idea. Y.W. and S.D. performed the measurements assisted by Y.D., L.S., X.G., X.Y., and Q.D. fabricated the MoS_2/WS_2 crystals. Y.W., S.D., Y.D., T.H., and Z.S. performed data analysis and wrote the manuscript. X.H., M.G., S.W., X.G., J.Z., and K.L. suggested the optical measurements. F.J.G.A. proposed the theoretical model. F.I. performed the theoretical calculations. All authors discussed the results and commented on the manuscript. All experimental works were done in Finland.

Notes

The authors declare no competing financial interest.

Acknowledgments

We thank Profs. Ermin Malic, Lijun Zhang, Thomas G. Pedersen, and Dr. Samuel Brem for their useful discussions. The authors acknowledge the financial support from Aalto Centre for Quantum Engineering, Academy of Finland (Grants: 312297, 312551, 314810, 333982, 336144 and 336818), Academy of Finland Flagship Programme (320167, PREIN), Youth Innovation Promotion Association CAS, the European Union's Horizon 2020 research and innovation program (Grant Agreement No. 820423, S2QUIP; 965124, FEMTOCHIP), National Natural Science Foundation of China (NSFC) (11634010, 51925203, 2022025, 51972074, 11674073, U2032206), the EU H2020-MSCA-RISE-872049 (IPN-Bio), China Scholarship Council, ERC (834742), Finnish Foundation for Technology Promotion (8216), the Spanish MINECO (MAT2017-88492-R and SEV2015-0522), the Catalan CERCA Program, and Fundació Privada Cellex, the Strategic Priority Research Program of the Chinese Academy of Sciences (XDB30000000, XDB360202), Youth Innovation Promotion Association CAS, and CAS Interdisciplinary Innovation Team (JCTD-2018-03).

References

(1) Boyd, R. W. Nonlinear Optics, 3rd ed.; Elseiver, 2007.

(2) Qi, J.; Yeganeh, M. S.; Koltover, I. I.; Yodh, A. G.; Theis, W. M. Depletion-electric-field-induced changes in second-harmonic generation from GaAs. Phys. Rev. Lett. 1993, 71 (4), 633−636.

(3) Johnson, J. C.; Knutsen, K. P.; Yan, H.; Law, M.; Zhang, Y.; Yang, P.; Saykally, R. J. Ultrafast carrier dynamics in single ZnO nanowire and nanoribbon lasers. Nano Lett. 2004, 4 (2), 197−204.

(4) Davidson, R. B.; Yanchenko, A.; Ziegler, J. I.; Avanesyan, S. M.; Lawrie, B. J.; Haglund, R. F. Ultrafast plasmonic control of second harmonic generation. ACS Photonics 2016, 3 (8), 1477−1481.

(5) Tisdale, W. A.; Williams, K. J.; Timp, B. A.; Norris, D. J.; Aydil, E. S.; Zhu, X.-Y. Hot-electron transfer from semiconductor nanocrytal. Science 2010, 328, 1543−1547.

(6) Jailaubekov, A. E.; Willard, A. P.; Tritsch, J. R.; Chan, W. L.; Sai, N.; Gearba, R.; Kaake, L. G.; Williams, K. J.; Leung, K.; Rossky, P. J.; Zhu, X. Y. Hot charge-transfer excitons set the time limit for charge separation at donor/acceptor interfaces in organic photovoltaics. Nat. Mater. 2013, 12 (1), 66−73.

(7) Goodman, A. J.; Dahod, N. S.; Tisdale, W. A. Ultrafast charge transfer at a quantum Dot/2D materials interface probed by second harmonic generation. J. Phys. Chem. Lett. 2018, 9 (15), 4227−4232.

(8) Novoselov, K. S.; Mishchenko, A.; Carvalho, A.; Castro Neto, A. H. 2D materials and van der Waals heterostructures. Science 2016, 353 (6298), aac9439.

(9) Autere, A.; Jussila, H.; Dai, Y.; Wang, Y.; Lipsanen, H.; Sun, Z. Nonlinear optics with 2D layered materials. Adv. Mater. 2018, 30 (24), 1705963.

(10) Wang, G.; Chernikov, A.; Glazov, M. M.; Heinz, T. F.; Marie, X.; Amand, T.; Urbaszek, B. Colloquium: Excitons in atomically thin transition metal dichalcogenides. Rev. Mod. Phys. 2018, 90 (2), No. 021001.

(11) Malard, L. M.; Alencar, T. V.; Barboza, A. P. M.; Mak, K. F.; de Paula, A. M. Observation of intense second harmonic generation from MoS2 atomic crystals. Phys. Rev. B: Condens. Matter Mater. Phys. 2013, 87 (20), 201401.

(12) Clark, D. J.; Senthilkumar, V.; Le, C. T.; Weerawarne, D. L.; Shim, B.; Jang, J. I.; Shim, J. H.; Cho, J.; Sim, Y.; Seong, M. J.; Rhim, S. H.; Freeman, A. J.; Chung, K. H.; Kim, Y. S. Strong optical nonlinearity of CVD-grown MoS2 monolayer as probed by wavelength- dependent second-harmonic generation. Phys. Rev. B: Condens. Matter Mater. Phys. 2014, 90 (12), 121409.

(13) Wang, G.; Marie, X.; Gerber, I.; Amand, T.; Lagarde, D.; Bouet, L.; Vidal, M.; Balocchi, A.; Urbaszek, B. Giant enhancement of the optical second-harmonic emission of WSe2 monolayers by laser excitation at exciton resonances. Phys. Rev. Lett. 2015, 114 (9), No. 097403.

(14) Wen, X.; Xu, W.; Zhao, W.; Khurgin, J. B.; Xiong, Q. Plasmonic hot carriers-controlled second harmonic generation in WSe2 bilayers. Nano Lett. 2018, 18 (3), 1686−1692.

(15) Dhakal, K. P.; Kim, H.; Lee, S.; Kim, Y.; Lee, J.; Ahn, J. H. Probing the upper band gap of atomic rhenium disulfide layers. Light: Sci. Appl. 2018, 7, 98.

(16) Lin, K.-Q.; Bange, S.; Lupton, J. M. Quantum interference in second-harmonic generation from monolayer WSe2. Nat. Phys. 2019, 15 (3), 242−246.

(17) Kumar, N.; Najmaei, S.; Cui, Q.; Ceballos, F.; Ajayan, P. M.; Lou, J.; Zhao, H. Second harmonic microscopy of monolayer MoS2. Phys. Rev. B: Condens. Matter Mater. Phys. 2013, 87 (16), 161403.

(18) Mennel, L.; Smejkal, V.; Linhart, L.; Burgdorfer, J.; Libisch, F.; Mueller, T. Band nesting in two-dimensional crystals: An exceptionally sensitive probe of strain. Nano Lett. 2020, 20 (6), 4242−4248.

(19) Mannebach, E. M.; Duerloo, K. A.; Pellouchoud, L. A.; Sher, M. J.; Nah, S.; Kuo, Y. H.; Yu, Y.; Marshall, A. F.; Cao, L.; Reed, E. J.; Lindenberg, A. M. Ultrafast electronic and structural response of monolayer MoS2 under intense photoexcitation conditions. ACS Nano 2014, 8 (10), 10734−10742.

(20) Jang, H.; Dhakal, K. P.; Joo, K. I.; Yun, W. S.; Shinde, S. M.; Chen, X.; Jeong, S. M.; Lee, S. W.; Lee, Z.; Lee, J.; Ahn, J. H.; Kim, H. Transient SHG imaging on ultrafast carrier dynamics of MoS2 nanosheets. Adv. Mater. 2018, 30 (14), 1705190.

(21) Seyler, K. L.; Schaibley, J. R.; Gong, P.; Rivera, P.; Jones, A. M.; Wu, S.; Yan, J.; Mandrus, D. G.; Yao, W.; Xu, X. Electrical control of second-harmonic generation in a WSe2 monolayer transistor. Nat. Nanotechnol. 2015, 10 (5), 407−411.

(22) Xiao, J.; Ye, Z.; Wang, Y.; Zhu, H.; Wang, Y.; Zhang, X. Nonlinear optical selection rule based on valley-exciton locking in monolayer WS2. Light: Sci. Appl. 2015, 4, e366.

(23) Yu, H.; Talukdar, D.; Xu, W.; Khurgin, J. B.; Xiong, Q. Chargeinduced second-harmonic generation in bilayer WSe2. Nano Lett. 2015, 15 (8), 5653−5657.

(24) Le, C. T.; Clark, D. J.; Ullah, F.; Jang, J. I.; Senthilkumar, V.; Sim, Y.; Seong, M.-J.; Chung, K.-H.; Kim, J. W.; Park, S.; Rhim, S. H.; Kim, G.; Kim, Y. S. Impact of selenium doping on resonant secondharmonic generation in monolayer MoS2. ACS Photonics 2017, 4 (1), 38−44.

(25) Taghinejad, M.; Xu, Z.; Wang, H.; Taghinejad, H.; Lee, K. T.; Rodrigues, S. P.; Adibi, A.; Qian, X.; Lian, T.; Cai, W. Photocarrierinduced active control of second-order optical nonlinearity in monolayer MoS2. Small 2020, e1906347.

(26) Dai, Y.; Wang, Y.; Das, S.; Xue, H.; Bai, X.; Hulkko, E.; Zhang, G.; Yang, X.; Dai, Q.; Sun, Z. Electrical Control of Interband Resonant Nonlinear Optics in Monolayer MoS2. ACS Nano 2020, 14 (7), 8442−8448.

(27) Wang, Y.; Ghotbi, M.; Das, S.; Dai, Y.; Li, S.; Hu, X.; Gan, X.; Zhao, J.; Sun, Z. Difference frequency generation in monolayer MoS2. Nanoscale 2020, 12 (38), 19638−19643.

(28) Ye, Z.; Cao, T.; O'Brien, K.; Zhu, H.; Yin, X.; Wang, Y.; Louie, S. G.; Zhang, X. Probing excitonic dark states in single-layer tungsten disulphide. Nature 2014, 513, 214−218.

(29) Quan, C.; Lu, C.; He, C.; Xu, X.; Huang, Y.; Zhao, Q.; Xu, X. Band alignment of MoTe2/MoS2 nanocomposite films for enhanced nonlinear optical performance. Adv. Mater. Interfaces 2019, 6 (5),

1801733.

(30) Wabnitz, S.; Eggleton, B. J. All-optical signal processing; Springer Series in Optical Sciences; Springer, 2015; Vol. 194.

(31) Cha, S.; Sung, J. H.; Sim, S.; Park, J.; Heo, H.; Jo, M. H.; Choi, H. 1s-intraexcitonic dynamics in monolayer MoS2 probed by ultrafast mid-infrared spectroscopy. Nat. Commun. 2016, 7, 10768.

(32) Shi, H.; Yan, R.; Bertolazzi, S.; Brivio, J.; Gao, B.; Kis, A.; Jena, D.; Xing, H. G.; Huang, L. Exciton dynamics in suspended monolayer and few-layer MoS2 2D crystals. ACS Nano 2013, 7 (2), 1072−1080.

(33) Ceballos, F.; Cui, Q.; Bellus, M. Z.; Zhao, H. Exciton formation in monolayer transition metal dichalcogenides. Nanoscale 2016, 8 (22), 11681−11688.

(34) Das, S.; Wang, Y. D.; Dai, Y. Y.; Li, S. S.; Sun, Z. P. Ultrafast transient sub-bandgap absorption of monolayer MoS2. Light: Sci. Appl. 2021, 10 (1), 27.

(35) Qiu, D. Y.; da Jornada, F. H.; Louie, S. G. Optical spectrum of MoS2: many-body effects and diversity of exciton states. Phys. Rev. Lett. 2013, 111 (21), 216805.

(36) Zhu, B.; Chen, X.; Cui, X. Exciton binding energy of monolayer WS2. Sci. Rep. 2015, 5, 9218.

(37) Pogna, E. A.; Marsili, M.; De Fazio, D.; Dal Conte, S.; Manzoni, C.; Sangalli, D.; Yoon, D.; Lombardo, A.; Ferrari, A. C.; Marini, A.; Cerullo, G.; Prezzi, D. Photo-induced bandgap renormalization governs the ultrafast response of single-layer MoS2. ACS Nano 2016, 10 (1), 1182−1188.

(38) Wang, Y. C.; Jons, K. D.; Sun, Z. P. Integrated photon-pair sources with nonlinear optics. Appl. Phys. Rev. 2021, 8 (1), No. 011314.

(39) Du, L. J.; Hasan, T.; Castellanos-Gomez, A.; Liu, G. B.; Yao, Y. G.; Lau, C. N.; Sun, Z. P. Engineering symmetry breaking in 2D layered materials. Nature Reviews Physics 2021, 3 (3), 193−206.

(40) Alloatti, L.; Palmer, R.; Diebold, S.; Pahl, K. P.; Chen, B.; Dinu, R.; Fournier, M.; Fedeli, J.-M.; Zwick, T.; Freude, W.; Koos, C.; Leuthold, J. 100 GHz silicon−organic hybrid modulator. Light: Sci. Appl. 2014, 3 (5), e173.

(41) Li, S.; Wang, S.; Tang, D.-M.; Zhao, W.; Xu, H.; Chu, L.; Bando, Y.; Golberg, D.; Eda, G. Halide-assisted atmospheric pressure growth of large WSe2 and WS2 monolayer crystals. Appl. Mater. Today 2015, 1 (1), 60−66.

(42) Giannozzi, P.; Baroni, S.; Bonini, N.; Calandra, M.; Car, R.; Cavazzoni, C.; Ceresoli, D.; Chiarotti, G. L.; Cococcioni, M.; Dabo, I.; Dal Corso, A.; de Gironcoli, S.; Fabris, S.; Fratesi, G.; Gebauer, R.; Gerstmann, U.; Gougoussis, C.; Kokalj, A.; Lazzeri, M.; Martin- Samos, L.; Marzari, N.; Mauri, F.;

Mazzarello, R.; Paolini, S.; Pasquarello, A.; Paulatto, L.; Sbraccia, C.; Scandolo, S.; Sclauzero, G.; Seitsonen, A. P.; Smogunov, A.; Umari, P.; Wentzcovitch, R. M. QUANTUM ESPRESSO: a modular and open-source software project for quantum simulations of materials. J. Phys.: Condens. Matter 2009, 21 (39), 395502.

(43) Perdew, J. P.; Burke, K.; Ernzerhof, M. Generalized gradient approximation made simple. Phys. Rev. Lett. 1996, 77 (18), 3865− 3868.

(44) Van Setten, M. J.; Giantomassi, M.; Bousquet, E.; Verstraete, M. J.; Hamann, D. R.; Gonze, X.; Rignanese, G. M. The PSEUDODOJO: Training and grading a 85 element optimized norm-conserving pseudopotential table. Comput. Phys. Commun. 2018, 226, 39−54.

(45) Hedin, L. New method for calculating the one-particle Green's function with application to the electron-gas problem. Phys. Rev. 1965, 139 (3A), A796.

(46) Onida, G.; Reining, L.; Rubio, A. Electronic excitations: density-functional versus many-body Green's-function approaches. Rev. Mod. Phys. 2002, 74 (2), 601−659.

(47) Marini, A.; Hogan, C.; Gruning, M.; Varsano, D. Yambo: an ab initio tool for excited state calculations. Comput. Phys. Commun. 2009, 180 (8), 1392−1403.

(48) Rohlfing, M.; Louie, S. G. Electron-hole excitations and optical spectra from first principles. Phys. Rev. B: Condens. Matter Mater. Phys. 2000, 62 (8), 4927−4944.

(49) Palummo, M.; Pulci, O.; Del Sole, R.; Marini, A.; Hahn, P.; Schmidt, W. G.; Bechstedt, F. The Bethe-Salpeter equation: a firstprinciples approach for calculating surface optical spectra. J. Phys. Condens. Matter 2004, 16 (39), S4313−S4322.

(50) Molina-Sanchez, A.; Sangalli, D.; Hummer, K.; Marini, A.; Wirtz, L. Effect of spin-orbit interaction on the optical spectra of single-layer, double-layer, and bulk MoS2. Phys. Rev. B: Condens. Matter Mater. Phys. 2013, 88 (4), No. 045412.

(51) Palummo, M.; Bernardi, M.; Grossman, J. C. Exciton radiative lifetimes in two-dimensional transit

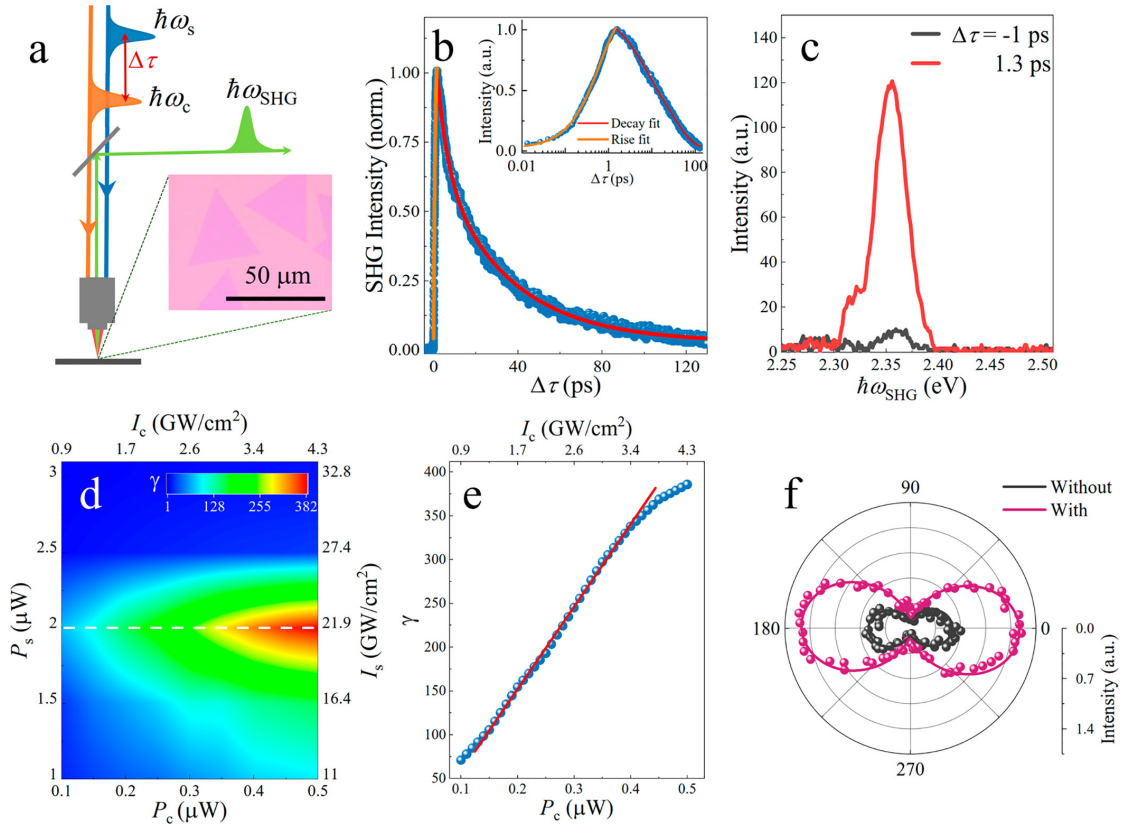

Figure 1. Giant SHG enhancement in MoS_2. (a) Sketch of the experimental setup. The inset shows an optical image of the probed MoS_2 flakes. **(b)** Normalized SHG intensity as a function of delay time Δτ. The average power of the control and seed light is ~0.5 and ~2 μW, respectively. The pulse duration is ~230 fs. The inset shows a semilog rendering of the same data. **(c)** SHG spectra before and after excitation with control light. **(d)** SHG enhancement factor γ as a function of input power/peak-intensity of the control (P_c, I_c) and seed (P_s, I_s) light. **(e)** Enhancement factor γ as a function of the control light power/intensity for P_s = 2 μW (data along the white dashed line in Figure 1d). **(f)** Polar plot of the circularly polarized SHG measured after passing a quarter-wave plate with and without the control light using σ- seed light. In (b)–(e), $\hbar\omega_c \approx 3.1$ eV. In (d)–(f), $\Delta\tau = 1.3$ ps. In (b)–(f), $\hbar\omega_{SHG} \approx 2.36$ eV.

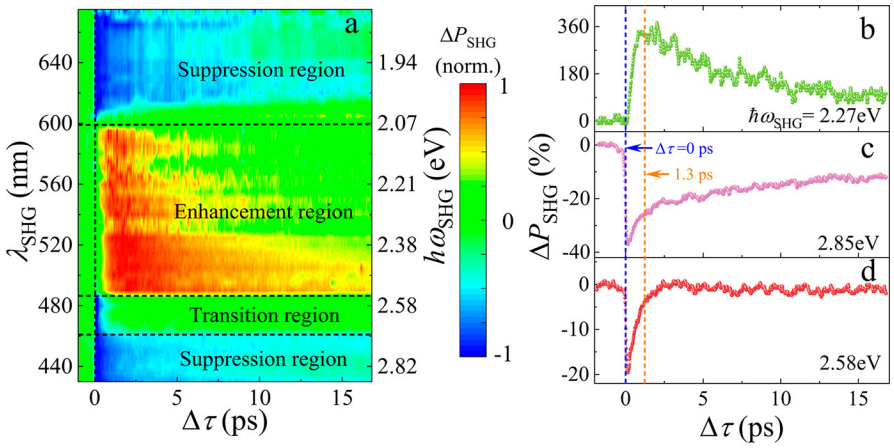

Figure 2. Broadband all-optical SHG modulation dynamics in MoS_2. (a) Normalized SHG change ΔP_{SHG} as a function of time delay and SHG photon wavelength/energy. The vertical black dashed line indicates the position of $\Delta\tau = 0$ ps. **(b–d)** ΔP_{SHG} response for $\hbar\omega_{SHG}$ ~2.27, 2.85, and 2.58 eV, respectively. Blue and orange dashed lines mark $\Delta\tau = 0$ and 1.3 ps. We use $I_c \approx 17.42$ GW/cm^2, $\hbar\omega_c \approx 1.55$ eV, and $I_s \approx 32.85$ GW/cm^2.

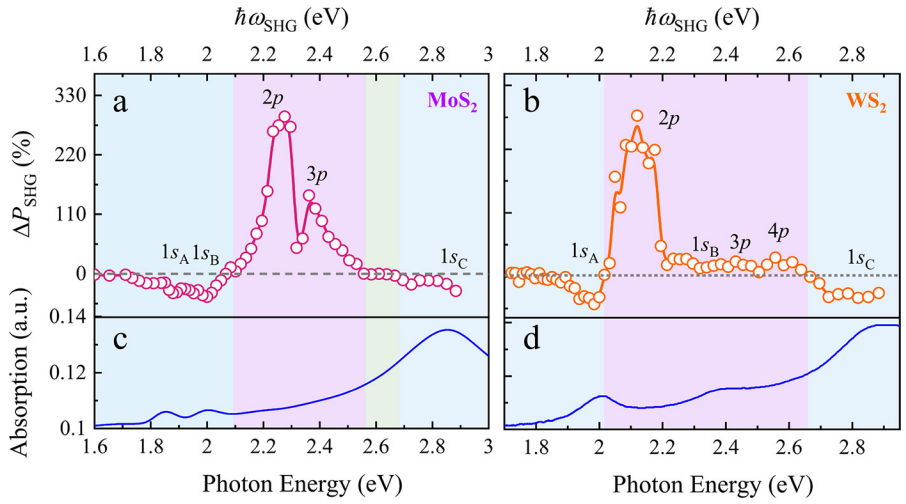

Figure 3. Maximum SHG modulation ΔP_{SHG} and optical absorption in monolayer MoS_2 and WS_2. (a) SHG change ΔP_{SHG} in monolayer MoS_2 for $\Delta\tau = 1.3$ ps, $\hbar\omega_c \approx 1.55$ eV, $I_c \approx 17.42$ GW/cm^2, and $I_s \approx 32.85$ GW/cm^2. **(b)** SHG change ΔP_{SHG} in monolayer WS_2 for $\Delta\tau = 2.8$ ps, $\hbar\omega_c \approx 3.1$ eV, $I_c \approx 2.57$ GW/cm^2, and $I_s \approx 32.85$ GW/cm^2. The gray dashed lines (zero value) and the solid curves connecting the dots are guides to the eye. **(c, d)** Linear optical absorption spectra of monolayer MoS_2 and WS_2, respectively. Different spectral regions are marked with background colors.

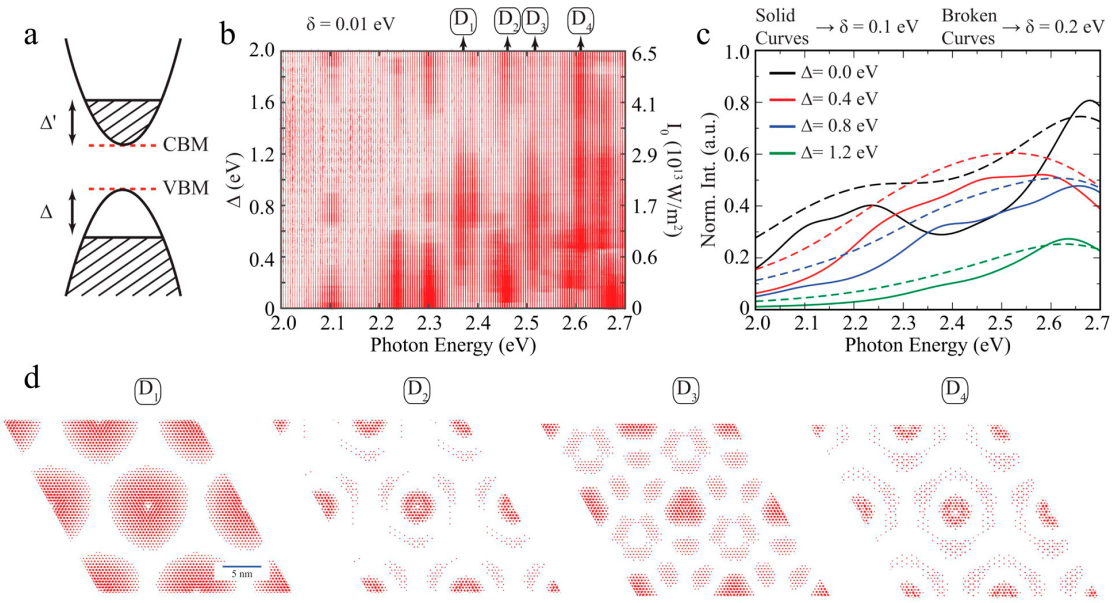

Figure 4. Theoretical interpretation of SHG modulation in monolayer MoS_2. (a) Schematic representation of the electronic bands of monolayer MoS_2 around the K point, showing an effective depletion region Δ produced upon optical pumping and a corresponding population of the conduction band up to an energy Δ′ adjusted to preserve the overall electron density. **(b)** Oscillator strength of excitonic states in the vicinity of the optically active region as a function of photon energy and Δ. **(c)** Spectrally resolved excitonic oscillator strength for Δ = 0, 0.4, 0.8, and 1.2 eV after introducing a photon energy broadening of 0.1 eV (solid curves) and 0.2 eV (broken curves). **(d)** Real-space wave functions of selected dark excitons, indicated by labels D_1–D_4 in Figure 4b, respectively.

Supplementary Materials for

- **Giant all-optical modulation of second-harmonic generation mediated by dark excitons**

Yadong Wang[1,2,†], Susobhan Das[2,†], Fadil Iyikanat[3,†], Yunyun Dai[2], Shisheng Li[4], Xiangdong Guo[5], Xiaoxia Yang[5], Jinluo Cheng[6], Xuerong Hu[2,7], Masood Ghotbi[8], Fangwei Ye[9], Harri Lipsanen[2], Shiwei Wu[10], Tawfique Hasan[11], Xuetao Gan[1], Kaihui Liu[12], Dong Sun[13], Qing Dai[5], F. Javier García de Abajo[3,14,*], Jianlin Zhao[1,*] and Zhipei Sun[2,15,*]

[1]MOE Key Laboratory of Material Physics and Chemistry under Extraordinary Conditions, and Shaanxi Key Laboratory of Optical Information Technology, School of Physical Science and Technology, Northwestern Polytechnical University, Xi'an 710129, China

[2]Department of Electronics and Nanoengineering, Aalto University, Espoo 02150, Finland

[3]ICFO-Institut de Ciencies Fotoniques, The Barcelona Institute of Science and Technology, 08860 Castelldefels (Barcelona), Spain

[4]International Center for Young Scientists, National Institute for Materials Science, Tsukuba, Japan

[5]Division of Nanophotonics, CAS Center for Excellence in Nanoscience, National Center for Nanoscience and Technology, Beijing 100190, China

[6]Changchun Institute of Optics, Fine Mechanics and Physics, Chinese Academy of Sciences, Changchun, Jilin, China.

[7]International Cooperation Base of Photoelectric Technology and Functional Materials, and Institute of Photonics and Photon-Technology, Northwest University, Xi'an 710069, China

[8]Department of Physics, University of Kurdistan, Pasdaran St., Sanandaj, Iran

[9]School of Physics and Astronomy, Shanghai Jiao Tong University, Shanghai 200240, China

[10]State Key Laboratory of Surface Physics, Key Laboratory of Micro and Nano Photonic Structures (MOE), and Department of Physics, Fudan University, Shanghai 200433, China

[11]Cambridge Graphene Centre, University of Cambridge, Cambridge CB3 0FA, UK.

[12]State Key Laboratory for Mesoscopic Physics and School of Physics, Peking University, Beijing 100871, China

[13]International Center for Quantum Materials, School of Physics, Peking University, Beijing 100871, China

[14]ICREA-Institució Catalana de Recerca i Estudis Avançats, Passeig Lluís Companys 23, 08010 Barcelona, Spain

[15]QTF Centre of Excellence, Department of Applied Physics, Aalto University, Espoo, Finland

[*]Emails: zhipei.sun@aalto.fi, jlzhao@nwpu.edu.cn, javier.garciadeabajo@nanophotonics.es

[†]Those authors contributed equally to this paper.

1. Experimental setup

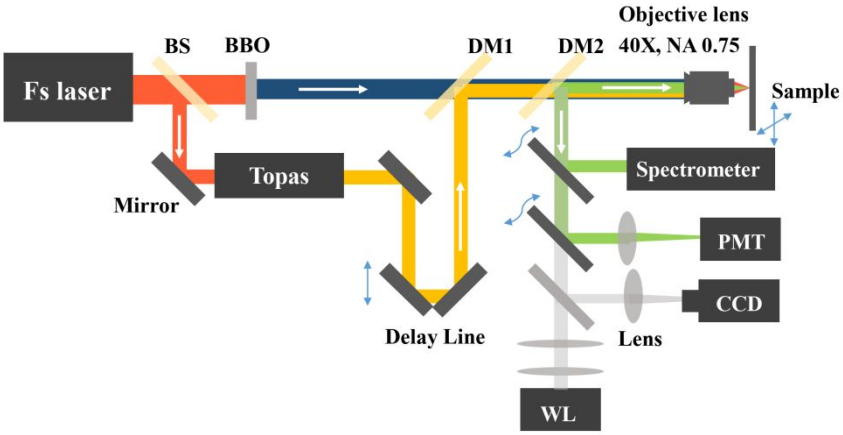

Fig. S1. Scheme of the experimental setup. The femtosecond laser source is Solstice Ace from Spectra-Physics. The TOPAS system is used for frequency conversion to produce the seed light with a wavelength range of 820-1600 nm. The control light wavelengths are either 400 nm or 800 nm. The pulse duration is ~230 fs and the repetition rate is 2 KHz. BBO: Beta barium borate; WL: white light for optical imaging of the sample; DM: dichroic mirror; BS: beam splitter; PMT: photomultiplier.

2. Monolayer MoS_2 sample characterization

The MoS_2 sample is prepared by chemical vapor deposition (CVD). Figure S2a shows a typical triangular flake deposited on a SiO_2/Si substrate. The Raman spectrum in Fig. S2b shows peaks at ~383 and 402 cm^{-1}, with a difference of 19 cm^{-1} identifying monolayer MoS_2. As shown in Fig. S2c, photoluminescence (PL) mapping shows that the MoS_2 layer is grown well and uniformly. Furthermore, the measured PL spectrum reveals two strong peaks at 620 nm and 670 nm (fitted by Lorentzians), corresponding to B and A excitons, respectively, as shown in Fig.

S2d. Photoluminescence and Raman spectra are measured under excitation with a continuous-wave laser of 532 nm wavelength and 0.8 μW incident power focused with a NA of 0.75.

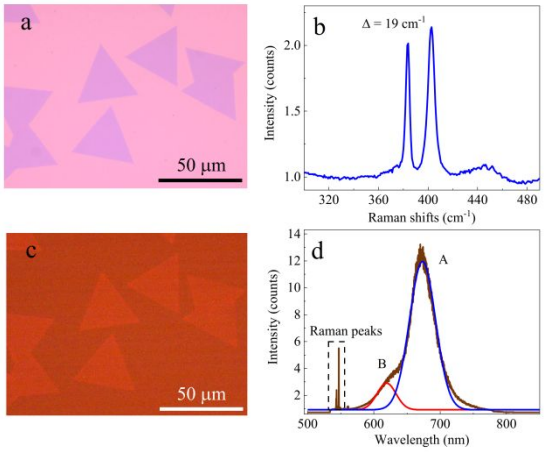

Fig. S2. CVD MoS_2 optical characterization. (a) Optical image. (b) Raman spectrum. (c) Photoluminescence mapping at the same position as in (a). (d) Photoluminescence spectrum.

3. Control and seed light power dependence of the SHG enhancement factor and time-resolved dynamics

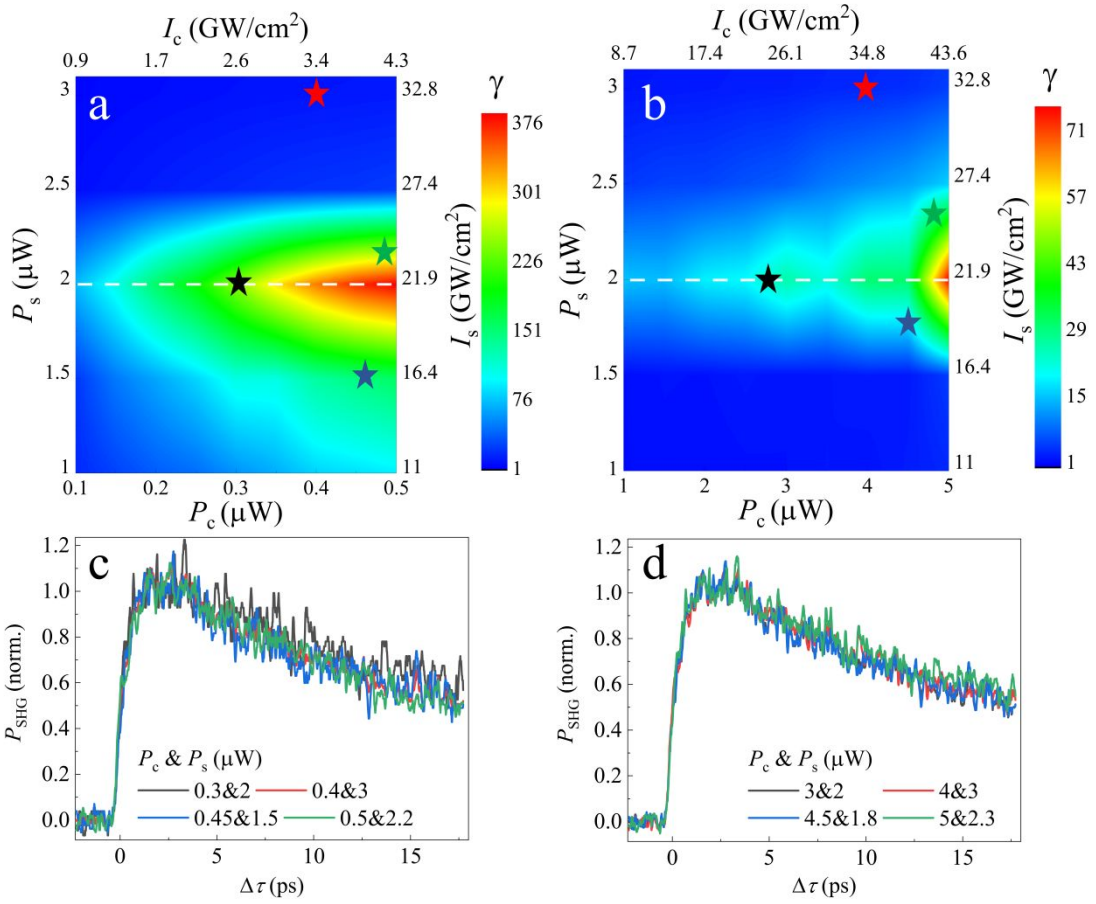

Fig. S3. (a,b) Power dependence of the enhancement factor γ for a control-seed delay $\Delta\tau$=1.3 ps with control light of wavelength λ_c =400 nm (a) and λ_c =800 nm (b). (c,d) Normalized P_{SHG} dynamics with different control light powers P_c and seed light powers P_s for λ_c = 400 nm (c) and λ_c = 800 nm (d). The dynamics of P_{SHG} is shown in (c) and (d), respectively The positions of stars in (a) and (b) correspond to different control and seed powers. The colors of stars and dynamics curves are coordinated.

4.Time-resolved ΔP_{SHG} dynamics in different regimes

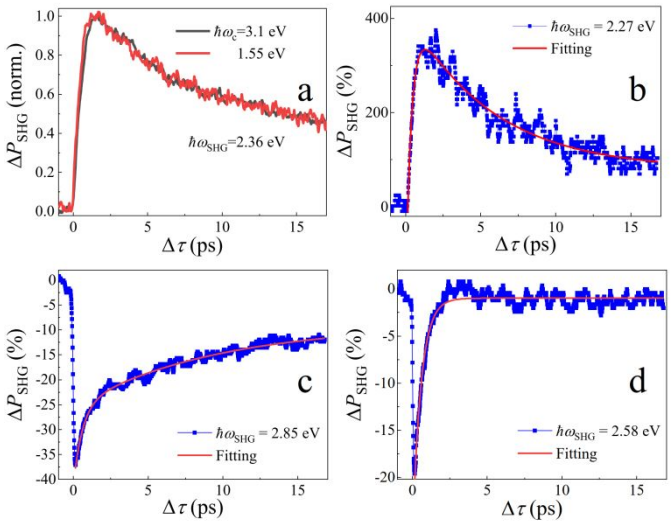

Fig. S4. (a) Time-resolved ΔP_{SHG} dynamics for two different control light photon energies (black: 3.1 eV; red: 1.55 eV) with seed light energy of 1.18 eV, which show a very similar transient response of ΔP_{SHG}. (b)-(d) Time-resolved ΔP_{SHG} dynamics with exponential fittings for three representative seed light energies in three different regimes: enhancement, suppression, and transition, respectively; the control light photon energy is fixed at 1.55 eV.

5. Photo-generation and recombination of charge carriers in transient ΔP_{SHG}

Figure S5 shows detailed measurements of carrier dynamics through ΔP_{SHG}. Figures S5a and S5c show the transient dynamics of ΔP_{SHG} when the SHG energies are 2.85 eV and 2.36 eV, respectively. The yellow curve is the sum frequency generation (SFG) measured under the same conditions to characterize the pulse duration. It shows that the drop time in Fig. S5a is much shorter than the control-seed light cross-correlation curve, while the decay time shows slower response, indicating the presence of different dynamical carrier processes. In contrast, in Fig. S5c ΔP_{SHG} at 2.36 eV photon energy initially rises until the delay time reaches $\Delta\tau$ = 1.3 ps, and then

it starts to decay. We note that the rise time is longer than the pulse duration. Figures S5b and S5d show the relationship between the control light power and the SHG signal for $\Delta\tau = 0.15$ ps (Fig. S5a) and 1.3 ps (Fig. S5c).

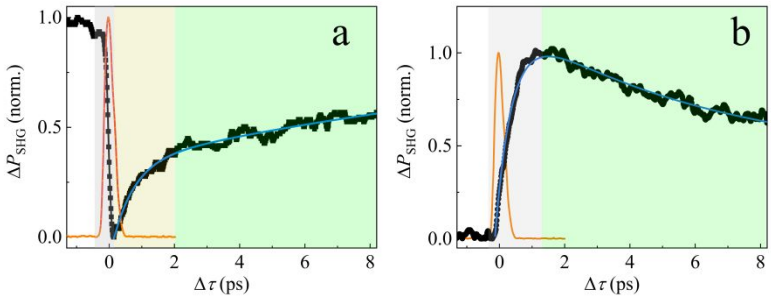

Fig. S5. Transient ΔP_{SHG} response for $\hbar\omega_{SHG}$ = 2.85 eV (a) and 2.36 eV (b) with the corresponding seed light photon energies at ~1.425 eV and 1.18 eV. The blue curves are exponential fittings of the decay processes. The orange curves indicate the signal of sum frequency generation (lying between the control light at 1.55 eV and the seed light), which is measured simultaneously during the all-optical modulation experiment. The peak positions of the sum frequency generation (orange curves) provide a good reference for the zero-time delay between the control and seed pulses.

6. Modulation of ΔP_{SHG} with control light power in the transition region

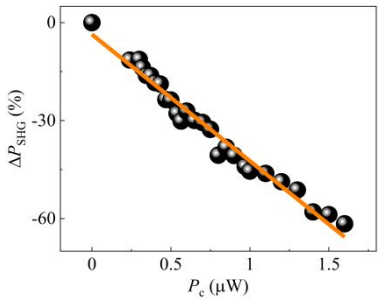

Fig. S6. Linear power dependence for $\hbar\omega_{SHG}$ = 2.58 eV and 2 μW average incident power of the seed light. The control light photon energy is $\hbar\omega_c$ = 3.1 eV.

7. Time-resolved ΔP_{SHG} spectra

In Figure S7, we plot results from SHG modulation spectroscopy at different time delays in the spectral range from ~2.16 to 2.88 eV. The spectra show very clear dynamics when $\Delta\tau$ varies from -1 to 10 ps (Fig. S7a-f). We observe that the enhancement peak positions remain unchanged when introducing control light, indicating that bandgap renormalization does not affect the sign of the change in SHG modulation. Furthermore, detailed spectra near the ΔP_{SHG}=0 condition are measured and shown in Fig. S7g, which shows blue shifts due to the evolution from the suppression region to the enhancement region.

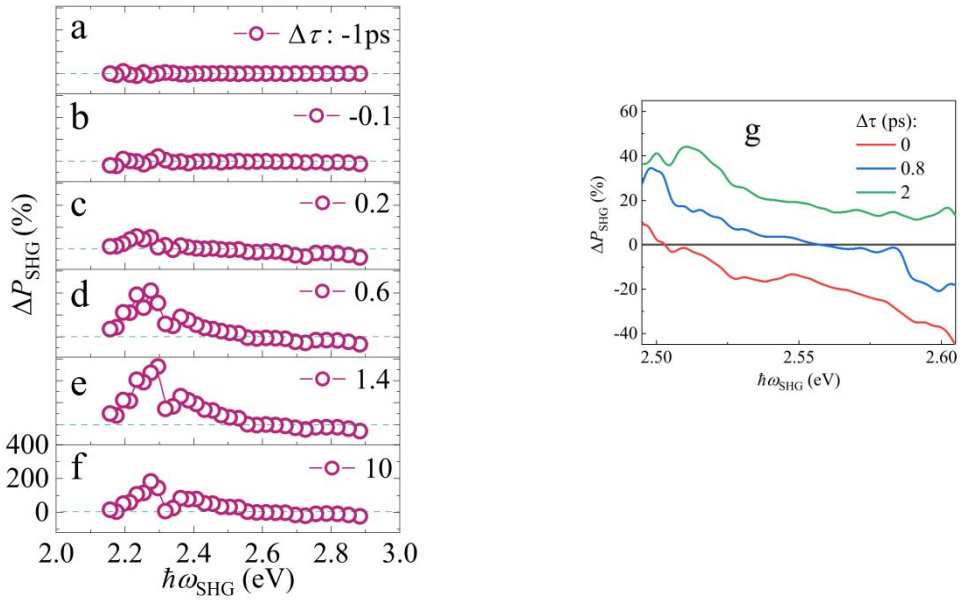

Fig. S7. (a)-(f) ΔP_{SHG} spectra at different delays $\Delta\tau$. (g) Blue shift of ΔP_{SHG} spectra at different time delays when $\hbar\omega_{SHG}$ lies in the transition region.

8. Comparison between SHG and ΔP_{SHG} in MoS_2

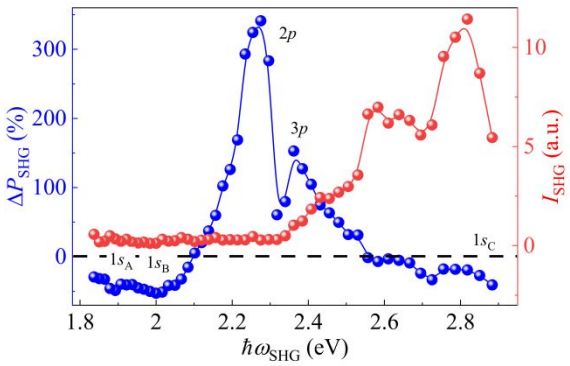

Fig. S8. Comparison between ΔP_{SHG} at $\Delta\tau = 1.1$ ps and the SHG responses of monolayer MoS_2. We attribute the larger SHG responses observed at higher photon energies (e.g., at 2.8 eV) to the C-exciton resonance.

9. MoS_2 field-effect transistor and electrically tunable all-optical modulation of SHG

It has been previously reported that exciton resonances and electrical doping can change the SHG response in monolayer TMDs.[1] We therefore investigate the possibility of electrical tunability of our observation of all optical SHG modulation. To this end, we have fabricated a MoS_2 field-effect transistor (Fig. S9a) for the experiments. The two electrodes are first patterned using electron-beam lithography (Vistec 5000+ES, Germany) and then covered with Ti (10 nm)/Au (60 nm) using an electron beam evaporation (OHMIKER-50B, Taiwan). The electrical performance of this device is shown in Fig. S9b. In particular, ΔP_{SHG} at the $1s_A$ exciton (1.89 eV energy) with different gate voltages (V_g) is shown in Fig. S9c. Figure S9d shows that the maximum $|\Delta P_{SHG}|$ varies from 43% to 25% at constant delay $\Delta\tau \approx 150$ fs when V_g increases from 0 to 100 V. These results indicate that electrical doping induces suppression of optical modulation, similar to the electrically tunable SHG behavior.[1] Electrical doping changes the Fermi level, which in turn influences the carrier occupation and thus the population of excitons.[1] Therefore, changing the doping level can eventually tune optical modulation of SHG in the material under investigation.

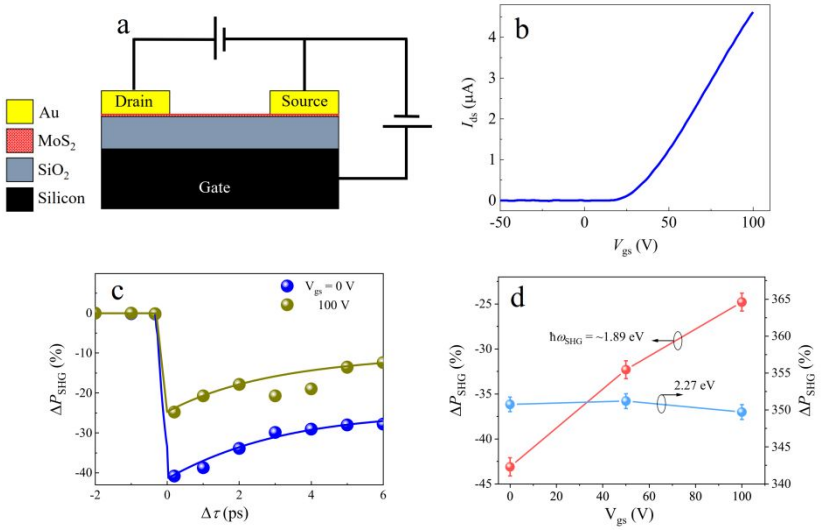

Fig. S9. (a) Schematic illustration of a MoS_2 field-effect transistor. (b) Source-drain current (I_{ds}) versus gate voltage (V_{gs}) when the drain voltage is fixed to $V_{ds} = 1$ V. (c) Optical modulation at different gate voltages for $\hbar\omega_{SHG} \approx 1.89$ eV. The applied seed and control light intensities are ~54.75 GW/cm^2 and ~17.42 GW/cm^2, respectively. (d) ΔP_{SHG} as a function of gate voltage when $\Delta\tau = \sim 150$ fs.

10. Preservation of MoS_2 symmetry with control light

We perform circularly-polarized SHG measurements in which circularly-polarized seed light is generated by combining a linear polarizer and a quarter-wave plate, focused on the monolayer MoS_2 with a sapphire substrate. The generated SHG is collimated with an objective lens and converted into linear polarization after going through another quarter-wave plate. Finally, a linear polarizer is employed to measure the polarization angle of the converted SHG signal.[2]

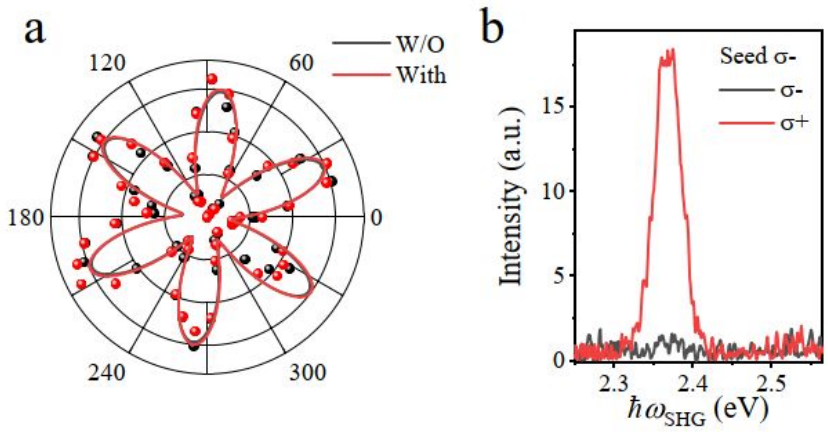

Fig. S10. (a) Polar plots of the normalized SHG intensity as a function of sample angle with (red curve) and without (black curve) pump excitation when the seed light is linearly polarized. (b) Circular polarization-resolved SHG spectra of the 3*p* excitonic state with excitation by a left-circularly-polarized seed laser (σ-).

11. Comparison of measured excitonic states with previous experimental results

TABLE S1. Comparison of exciton energies in monolayer MoS_2.

Exciton	Energy from Ref. 3 (eV)	Energy from ΔP_{SHG} (eV)※	Energy from the linear reflection (eV)
$1s_A$	1.86	1.89	1.9
$2p_A$	-	-	-
$3p_A$	2.13	-	-
$1s_B$	2.01	2.0	2.05
$2p_B$	2.22	2.27	-
$3p_B$	2.37	2.36	-
$1s_C$	-	2.9	2.93

※This work

12. Sign change in the enhancement and suppression regions for various SHG wavelengths

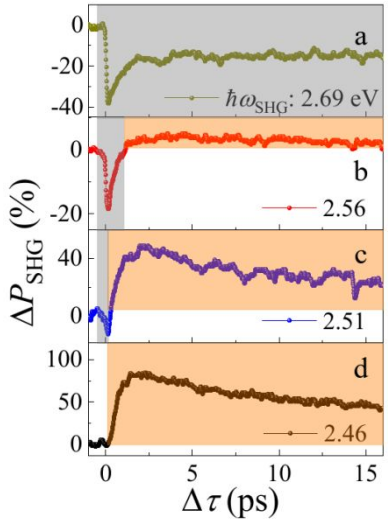

Fig. S11. (a)-(d) ΔP_{SHG} responses when varying $\hbar\omega_{\mathrm{SHG}}$ in the 2.46-2.69 eV range. Negative and positive signs are indicated by grey and orange regions.

13. Theoretical calculation of the change in second-order nonlinear susceptibility

The modulation of the SHG signal before and after the arrival of a control light pulse can be explained as the change in the second-order nonlinear susceptibility of the system $\chi^{(2)}$. The power of the SHG signal generated from the seed light in the absence of control light (p_0) or in the presence of control light (p_c) can be expressed as

$$p_0 \propto \left(\chi_0^{(2)}\right)^2$$

$$p_c \propto \left(\chi_c^{(2)}\right)^2$$

where $\chi_c^{(2)}$ and $\chi_0^{(2)}$ are the corresponding second-order nonlinear susceptibilities of monolayer MoS_2 at the seed wavelength with and without control light, respectively.

From here, the relative change in second-order nonlinear susceptibility can be expressed as

$$\frac{\Delta\chi^{(2)}}{\chi_0^{(2)}} = \frac{\chi_c^{(2)} - \chi_0^{(2)}}{\chi_0^{(2)}} = \sqrt{\frac{p_c}{p_0}} - 1$$

In the enhancement region, we find a maximum relative change in second.order nonlinear susceptibility of ~19.

14. Supplementary theoretical elements in the analysis of SHG modulation

We use the GW-BSE method to calculate the absorption spectrum of monolayer MoS_2. This method yields reliable predictions for the excited-state properties of ultra-thin transition metal dichalcogenides.[4, 5] In Fig. S12a, we represent the electronic band structure calculated within the GGA and G_0W_0 approximations for monolayer MoS_2, showing that inclusion of quasiparticle energy corrections to the Kohn-Sham eigenvalues (i.e., when moving from GGA to G_0W_0) leads to a direct band gap of 2.77 eV at the K point.

We obtain the absorbance spectrum of monolayer MoS_2 from the imaginary part of the dielectric function, as shown in Fig. S12b, which reveals several excitonic features located below the band gap of the material with high oscillator strengths. A comparison of the spectral peak positions of the experimentally observed and theoretically predicted bright excitonic states is presented in Table S2. The 0.25 eV redshift of the calculated peak positions relative to experiment can be attributed to the error margin of the GW-BSE approach.[6] In addition, we show the variation of band gap and binding energy of the two lowest-energy excitons ($1s_A$ and $1s_B$) with respect to the size of the *k*-point mesh and the number of bands in Fig. S13.

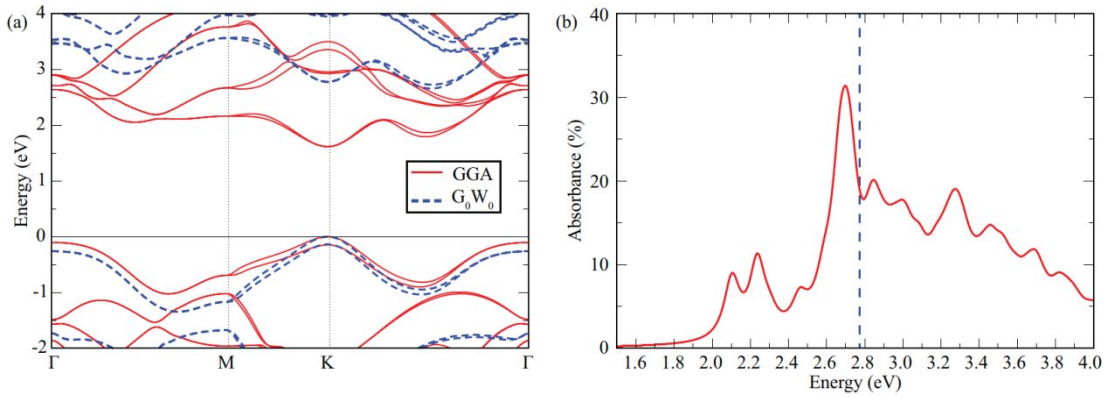

Fig. S12. (a) Electronic bands of monolayer MoS_2 calculated in the GGA and G_0W_0 approximations. (b) Absorbance of monolayer MoS_2 computed within the G_0W_0–BSE approximation.

TABLE S2. Comparison of experimental and theoretical exciton energies in monolayer MoS_2.

	$1s_A$	$1s_B$	$2p_A$	$2s$	$3p_A$	$2p_B$	$3s$	$3p_B$
Bright(B)/Dark(D)	B	B	D_1	B	D_2	D_3	B	D_4
Experiment (eV)	1.85	2.00	-	2.19	-	2.27	2.36	2.37
Calculation (eV)	2.10	2.24	2.37	2.44	2.46	2.52	2.59	2.59

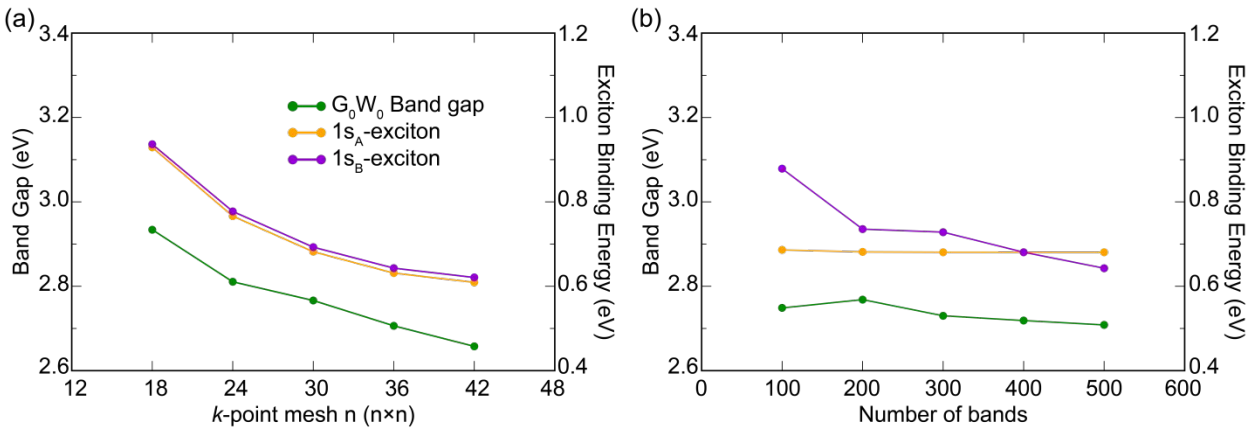

Fig. S13. Convergence of the direct band gap at the K-point and the binding energies of $1s_A$ and $1s_B$ excitons with respect to (a) the size of the *k*-point mesh and (b) the number of bands. In each panel, left and right scales show the band gap and exciton binding energies, respectively.

15. SHG modulation with monolayer WS_2

A typical WS_2 sample characterization is shown in Fig. S14.

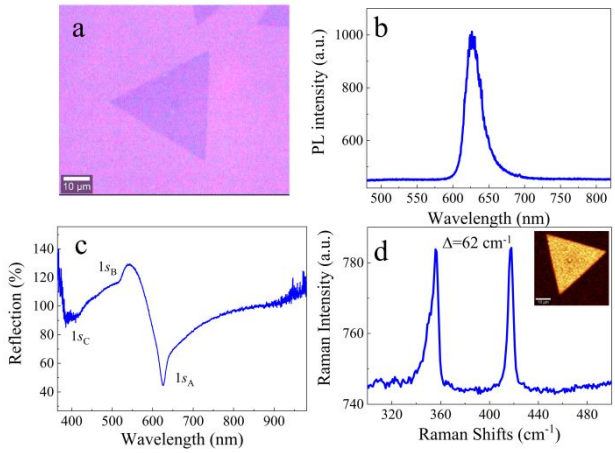

Fig. S14. CVD WS_2 sample characterization. (a) Optical image. (b) Photoluminescence spectrum. (c) Optical reflectance. (d) Raman spectrum with an excitation wavelength of 488 nm. Inset: Raman map of the 336 cm^{-1} shifted peak.

Our measurements of SHG modulation in WS_2 are carried out with the same system employed for MoS_2 using control light of 400 nm wavelength (3.1-eV photon energy). Figure S15a shows the dependence of SHG enhancement γ on the power of control and seed light (1170 nm, 1.05 eV). Clearly, the SHG enhancement factor γ increases with increasing control light power, whereas it decreases with increasing seed light power. Figure S15b shows γ as a function of control light power when the seed light power is 1 μW, from which we conclude that γ can be as high as ~76 when the control light power is 0.3 μW.

The normalized ΔP_{SHG} is shown in Fig. S16 as a function of time delay for different seed light wavelengths. The incident powers of the seed light and control light are 3 μW and 0.3 μW, respectively. As shown in Fig. S16a, the time-resolved ΔP_{SHG} dynamics with various SHG energies clearly reveals the presence of suppression, transition, and enhancement regions. The results of SHG modulation presented in Fig. S16b-e show very similar dynamics when compared to those for MoS_2 at different regions.

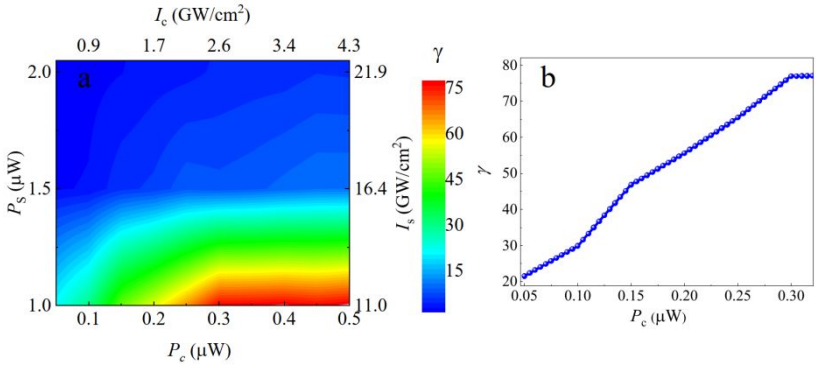

Fig. S15. (a) SHG enhancement factor γ as a function of input power/peak-intensity of the control (P_c, I_c) and seed (P_s, I_s) light in WS_2. (b) γ as a function of control light power for a seed light power of 1 μW.

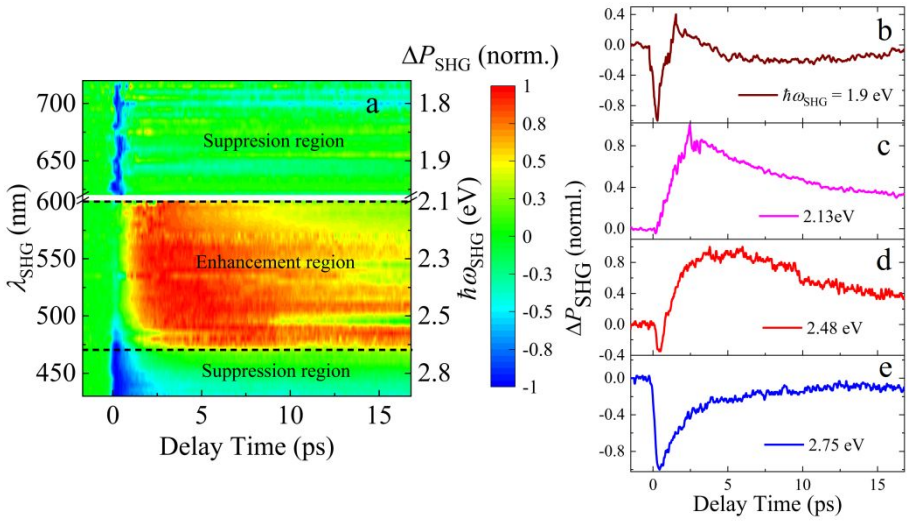

Fig. S16. All-optical modulation dynamics in monolayer WS_2. (a) Normalized SHG power change ΔP_{SHG} as a function of time delay and SHG photon wavelength/energy. The breaking region signals the overlap between difference frequency generation and SHG. (b)-(e) ΔP_{SHG} dynamics for $\hbar\omega_{SHG}$ = 1.9, 2.13, 2.48, and 2.75 eV, respectively.

TABLE S3. Comparison of exciton energies in monolayer WS_2.

	$1s_A$	$2p$	$1s_B$	$3p$	$4p$	T
Ref. S5	2.04	2.28	2.45	2.48		10k
Ref. S7	2.12	*	2.50	*	*	10k
Ref. S7	2.02	*	2.40	2.45	2.58	300k
Linear	1.98	*	2.39	*	*	300k
ΔP_{SHG}	1.98	2.11	*	2.43	2.58	300k

Supplementary References

(S1) Seyler, K. L.; Schaibley, J. R.; Gong, P.; Rivera, P.; Jones, A. M.; Wu, S.; Yan, J.; Mandrus, D. G.; Yao, W.; Xu, X., Electrical control of second-harmonic generation in a WSe_2 monolayer transistor. *Nat. Nanotechnol.* **2015**, *10* (5), 407-11.

(S2) Zhang, D.; Zeng, Z.; Tong, Q.; Jiang, Y.; Chen, S.; Zheng, B.; Qu, J.; Li, F.; Zheng, W.; Jiang, F.; Zhao, H.; Huang, L.; Braun, K.; Meixner, A. J.; Wang, X.; Pan, A., Near-Unity Polarization of Valley-Dependent Second-Harmonic Generation in Stacked TMDC Layers and Heterostructures at Room Temperature. *Adv. Mater.* **2020**, *32* (29), e1908061.

(S3) Cha, S.; Sung, J. H.; Sim, S.; Park, J.; Heo, H.; Jo, M. H.; Choi, H., 1s-intraexcitonic dynamics in monolayer MoS_2 probed by ultrafast mid-infrared spectroscopy. *Nat. Commun.* **2016**, *7*, 10768.

(S4) Qiu, D. Y.; da Jornada, F. H.; Louie, S. G., Optical spectrum of MoS_2: many-body effects and diversity of exciton states. *Phys. Rev. Lett.* **2013**, *111* (21), 216805.

(S5) Ye, Z.; Cao, T.; O'Brien, K.; Zhu, H.; Yin, X.; Wang, Y.; Louie, S. G.; Zhang, X., Probing excitonic dark states in single-layer tungsten disulphide. *Nature* **2014**, *513*, 214.

(S6) Molina-Sanchez, A.; Sangalli, D.; Hummer, K.; Marini, A.; Wirtz, L., Effect of spin-orbit interaction on the optical spectra of single-layer, double-layer, and bulk MoS_2. *Phys. Rev. B* **2013**, *88* (4), 045412.

(S7) Zhu, B.; Chen, X.; Cui, X., Exciton binding energy of monolayer WS_2. *Sci Rep-Uk* **2015**, *5*, 9218.